Journal of The Electrochemical Society, 2023 **170** 050510
1945-7111/2023/170(5)/050510/11/$40.00 © 2023 The Electrochemical Society ("ECS"). Published on behalf of ECS by IOP Publishing Limited

Screening of Electrolyte-Anode Buffers to Suppress Lithium Dendrite Growth in All-Solid-State Batteries

Weiyu Li, Hamdi A. Tchelepi, and Daniel M. Tartakovsky[z]

Department of Energy Science and Engineering, Stanford University, Stanford, California 94305, United States of America

Dendritic growth of lithium (Li) metal is a leading cause of degradation and catastrophic failure of all-solid-state batteries (ASSBs) with Li anode. Insertion of a buffer layer between the Li-metal and the solid electrolyte is known to ameliorate this phenomenon; yet the identification of an optimal buffer material, and the design of ASSBs that can be manufactured at scale, remains elusive and largely driven by trial-and-error experimentation. Our analysis seeks to accelerate the buffer-materials discovery by elucidating the conditions under which the buffer's presence stabilizes electrodeposition on the Li anode in ASSBs. The analysis quantifies the interfacial instability associated with dendrite formation in terms of the battery's operating conditions and the electrochemical and physical properties of the buffer material and solid electrolyte. The model predicts that, among several prospective buffer materials, Ag, Al, Sn and antiperovskite super ionic conductor, $Li_3S(BF_4)_{0.5}Cl_{0.5}$, are effective in stabilizing electrodeposition and suppressing dendrite growth. Our model's predictions of the dendrite suppression abilities of different buffer materials are consistent with the published experimental findings. The model can be used to guide experimental and computational discovery of new buffer materials that match a particular electrolyte.
 [DOI: 10.1149/1945-7111/acd0da]

Manuscript submitted January 14, 2023; revised manuscript received March 19, 2023. Published May 5, 2023.

All-solid-state lithium-metal batteries (ASSBs) hold the promise of becoming the next-generation safe, high-capacity power source for electric vehicles. In ASSBs, the flammable organic liquid electrolyte currently used in lithium-ion and lithium-metal batteries is replaced with either an organic solid polymer electrolyte or an inorganic solid ceramic/glass electrolyte. Solid ceramic electrolytes, such as the garnet-type $Li_7La_3Zr_2O_{12}$ (LLZO),[1] have attracted a lot of attention due to their superior ionic conductivity, high mechanical strength, and chemical stability with respect to lithium (Li) metal. However, their widespread adoption is impeded by manufacturing challenges and poor electrode/electrolyte interfacial contact. Crucially, formation and growth of Li dendrites are the leading causes of ASSB degradation,[2,3] just as they are for Li-metal batteries.

Proposed strategies for suppression of Li-dendrite growth in ASSBs include use of single-crystal solid ceramic electrolytes, fabrication of pallets with high density and few defects, development of composites combining a solid ceramic electrolyte with a self-healing polymer, and optimization of the Li-metal (Table I in Ref. 4). Our study focuses on arresting the Li-dendrite initiation by stabilizing the Li-metal/electrolyte interface.[4] This goal is accomplished by introducing a buffer layer between the Li-metal electrode and the solid ceramic electrolyte. For example, the placement of an aluminum (Al), silicon (Si), germanium (Ge), aluminum oxide (Al_2O_3), lithium nitride (Li_3N), or Li-rich anti-perovskite (Li_3OCl) buffer layer between Li-metal and garnet electrolyte has been shown experimentally to prevent dendrite growth.[4] In the same vein, an electronic-insulating lithium fluoride (LiF) interfacial layer has been shown to facilitate the physical contact between Li-metal and LLZTO ($Li_{6.4}La_3Zr_{1.4}Ta_{0.6}O_{12}$) electrolyte and promote uniform Li-plating/stripping.[5] The same positive outcome is achieved by either screen-printing silver (Ag) on the garnet electrolyte of an ASSLB,[6] or silver-coating the Li-metal surface of a Li-metal battery.[7] Both approaches result in stable Li-plating/stripping profiles at different current densities.

Most of the experimental exploration of potential buffer materials is chemistry-driven and uninformed by quantitative predictions of Li-ion (Li^+) transport and electrochemical transformations in the solid ceramic electrolyte and the buffer. Theoretical and computational work on this subject is scarce.[8,9] It includes a physics-based model of the electrochemical potential in an ASSB, which accounts for mixed ionic and electronic conduction through the solid electrolyte and buffer layer, but neglects interface resistances and resulting electrode overpotentials.[10] An example of statistical models is a computational screening of over 12,000 inorganic solids, in which machine learning techniques are used to correlate the stability of electrodeposition to various mechanical properties of solid electrolytes.[11] Statistical studies of this kind provide little physical insight that can inform materials or battery design.

We fill this void by presenting a mathematical model of electrodeposition on the Li anode in ASSBs with a buffer layer between the Li anode and the solid ceramic electrolyte. The model describes Li^+ transport in the electrolyte and the buffer, in the presence of an interfacial charge-transfer reaction. We analyze two kinds of buffer material: electronic conductors (e.g., Al and Ag) and electronic insulators (e.g., Al_2O_3, Li_3N, Li_3OCl and LiF); buffers composed of semiconductors (e.g., Si and Ge) are left for future study. Conditions favorable to the onset of dendritic growth or, conversely, to its suppression are established by means of a linear stability analysis of this model.

Our analysis leads to analytical expressions that relate the dendrite growth rate to measurable characteristics such as buffer's thickness and surface morphology, current density, transport properties (Li^+ diffusivity, ionic conductivity) of the electrolyte and the buffer, and the interfacial energy between the Li-metal and the solid electrolyte or buffer layer. This analysis identifies effective buffer materials, which can have either high electronic conductivity (Ag, Al, and tin Sn) or low electronic conductivity (anti-perovskite, $Li_{2.99}Ba_{0.005}OCl$[12] and $Li_3S(BF_4)_{0.5}Cl_{0.5}$,[13] both of which are super ionic conductors). Such results provide a useful screening tool to narrow down the space of plausible candidates for an optimal dendrite-suppression buffer material. Ultimate selection of the ideal candidate would be determined by additional factors (e.g., elastic properties and geographic scarcity) absent from our model, such as the mode of a material's application (e.g., coating or construction of a composite) and economic cost.

Mathematical Formulation

We consider electrodeposition on the Li-metal anode, Ω_{an}, that is separated from the solid electrolyte, Ω_{el}, by the thin buffer layer Ω_b; our model of an ASSB is two-dimensional and deals with the half-cell domain in Fig. 1. A negative electrostatic potential, ϕ_e, is maintained on the Li-metal electrode surface, $\Gamma(t)$, at all time t; the electric potential at the outer edge of the electrolyte ($x = L$) is fixed at 0. The Li-metal electrode surface, $\Gamma(t)$, is initially (at time $t = 0$)

[z]E-mail: tartakovsky@stanford.edu

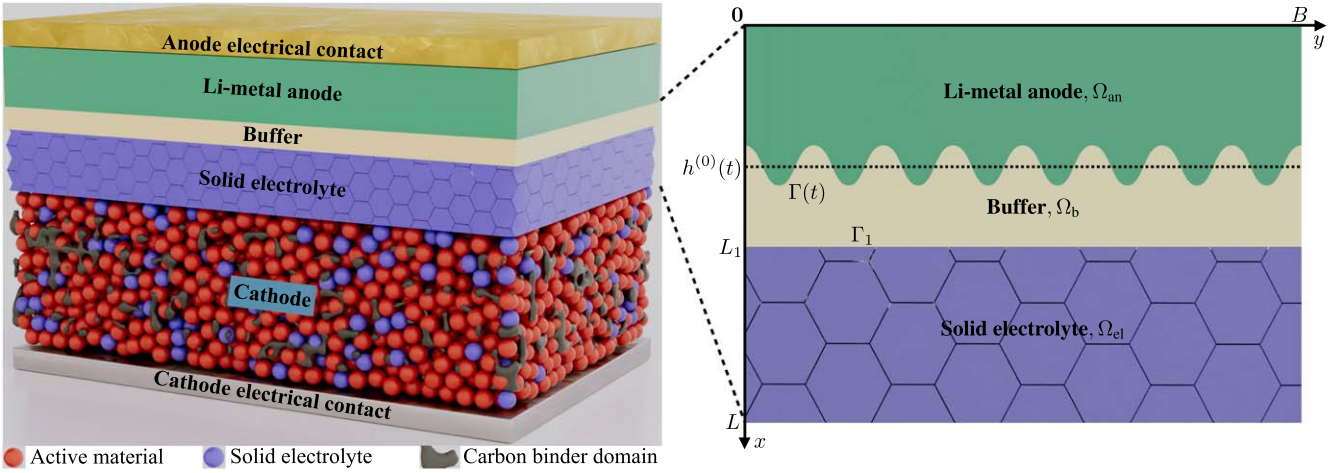

Figure 1. Schematic representation of an ASSB (Left) and the two-dimensional half-cell domain considered in this study (Right). The half cell consists of the Li-metal anode, Ω_{an}, that is separated from the solid electrolyte, Ω_{el}, by the buffer layer Ω_b. The anode's surface $\Gamma(t)$ evolves with time t due to electrodeposition, while the interface Γ_1 between Ω_{el} and Ω_b remains fixed.

flat and coincides with the plane $x = 0$, i.e., $\Gamma(0) = \{\mathbf{x} = (x, y)^\top : x = 0,\ 0 \leqslant y \leqslant B\}$.

Temporal evolution of the Li-metal surface $\Gamma(t)$ is a result of electrodeposition that involves a Faradaic reaction between cations (Li^+) and electrons (e^-), $Li^+ + e^- \rightarrow Li$, which results in the formation of Li atoms that are subsequently deposited on Γ. Depending on the ratio between the buffer electronic conductivity, σ_{e^-}, and the ionic conductivity for Li^+, σ_{Li^+}, this reaction takes place on either the anode-buffer interface $\Gamma(t)$ or the buffer-electrolyte interface Γ_1 (Fig. 1). For buffer materials with $\sigma_{e^-} \gg \sigma_{Li^+}$ (Scenario 1), the Faradaic reaction takes place on Γ_1 and the resultant Li atoms are transported to $\Gamma(t)$ by diffusion; for buffer materials with $\sigma_{e^-} \ll \sigma_{Li^+}$ (Scenario 2), the Faradaic reaction occurs on $\Gamma(t)$. We consider both scenarios.

We ignore mechanical effects, e.g., solid electrolyte fracture, rupture of the coated layer, etc., and explore Li diffusion in the buffer layer as a possible dendrite-stabilization mechanism.

Governing equations.—We use a two-dimensional Cartesian coordinate system spanned by the orthogonal unit-vectors $\mathbf{e}_x$ and $\mathbf{e}_y$, and represent the anode surface with dendrites, $\Gamma(t)$, by a single-valued function $h(y, t)$ such that $h(y, 0) = 0$ (Fig. 1). The unit-normal vector, $\mathbf{n}(y, t)$, and mean curvature, $\kappa(y, t)$, of the anode surface $\Gamma(t)$ are computed as[14]

$$\mathbf{n} = \frac{1}{\sqrt{1 + (\partial_y h)^2}} \begin{pmatrix} -1 \\ \partial_y h \end{pmatrix}, \qquad \kappa = -\frac{1}{2} \frac{\partial_y^2 h}{[1 + (\partial_y h)^2]^{3/2}}. \qquad [1]$$

We analyze the stability of electrodeposition in order to identify the conditions under which a small perturbation of $h(y, t)$ dissipates (rather than grows) with time t.

The rate of change of $\Gamma(t)$ or, equivalently, $h(y, t)$ is given by the normal component of the mass flux of Li atoms, $\mathbf{J}^b_{Li}(\mathbf{x}, t)$ (mol/m^2/s), across the buffer/anode interface:

$$\mathbf{e}_x \cdot \mathbf{n} \frac{\partial h}{\partial t} = -\omega \mathbf{n} \cdot \mathbf{J}^b_{Li}, \qquad \mathbf{x} \in \Gamma(t), \qquad [2]$$

where ω is the molar volume of Li-metal (m^3 mol^{-1}). The flux $\mathbf{J}^b_{Li}(\mathbf{x}, t)$ is computed from the mass and charge conservation laws for both the buffer and the electrolyte.

Solid electrolyte.—The Li cations, Li^+, are the only mobile species in the solid electrolyte, $\Omega_{el} = \{\mathbf{x}: L_1 < x < L,\ 0 \leqslant y \leqslant B\}$. Experimental evidence suggests that these cations are distributed almost uniformly throughout the electrolyte so that their concentration $c^{el}_{Li^+}$ is approximately constant and equal to the initial concentration in the electrolyte, $c^{el}_{Li^+}(\mathbf{x}, t) \approx c_0$; hence, its gradient is $\nabla c^{el}_{Li^+} \approx \mathbf{0}$ and their diffusion flux is negligible.[15,16] Consequently, in our model, the movement of Li^+ is entirely due to electromigration. The Nernst-Planck expression for the Li^+ flux in the electrolyte reduces to $\mathbf{J}^{el}_{Li^+} = -zFu_{el}c_0\nabla\varphi_{el}$, where z is number of proton charges carried by Li^+, F is the Faraday constant (s · A/mol), $\phi_{el}(\mathbf{x})$ is the electric potential in the electrolyte (V), and u_{el} is the mobility of Li^+ in the electrolyte due to the potential gradient $\nabla\phi_{el}$. In the absence of an externally imposed magnetic field, the current density $\mathbf{i}_{el}(\mathbf{x})$ is related to the ionic flux $\mathbf{J}^{el}_{Li^+}(\mathbf{x})$ by[15] $\mathbf{i}_{el} = zF\mathbf{J}^{el}_{Li^+}$. This gives rise to Ohm's law and charge conservation in the solid electrolyte,[17,18]

$$\mathbf{i}_{el} = -\sigma_{el}\nabla\varphi_{el} \quad \text{and} \quad \nabla \cdot \mathbf{i}_{el} = 0, \quad \mathbf{x} \in \Omega_{el}, \qquad [3]$$

where $\sigma_{el} = z^2F^2u_{el}c_0$ is the electrolyte's ionic conductivity for Li^+ (S m^{-1}).

Equation 3 are subject to the boundary conditions

$$\varphi_{el}(L, y) = 0, \qquad \frac{\partial\varphi_{el}}{\partial y}(x, 0) = \frac{\partial\varphi_{el}}{\partial y}(x, B) = 0, \qquad [4]$$

the last two of which represent the electrically insulated vertical surfaces, $y = 0$ and B. The boundary conditions on the electrolyte/buffer interface $\Gamma_1 = \{\mathbf{x}: x = L_1,\ 0 \leqslant y \leqslant B\}$ are determined by the material properties of the buffer, as detailed below.

Buffer layer.—The thin buffer, initially of uniform thickness L_1, is represented by the domain $\Omega_b(t) = \{\mathbf{x}: h(y, t) < x < L_1,\ 0 < y < B\}$. The buffer is characterized by its conductivities for electrons (σ_{e^-}) and Li^+ (σ_{Li^+}). We consider two limiting cases defined by the magnitude of the ratio $\sigma_{e^-}/\sigma_{Li^+}$.

Scenario 1: Buffer with high electronic conductivity. In buffers with $\sigma_{e^-} \gg \sigma_{Li^+}$ (e.g., Al and Ag), the electron concentration is high and approximately constant throughout the buffer, so that the electric potential in the buffer, ϕ_b, is constant as well. Consequently, the Li^+ ions undergo the Faradaic reaction at the buffer/electrolyte interface, $x = L_1$, and reduce to the Li atoms that subsequently

diffuse in Ω_b and are deposited on the anode surface $\Gamma(t)$. The spatiotemporal evolution of the molar concentration of Li atoms, $c_{Li}^b(\mathbf{x}, t)$ (mol m^{-3}), is described by the diffusion equation

$$\frac{\partial c_{Li}^b}{\partial t} = -\nabla \cdot \mathbf{J}_{Li}^b, \qquad \mathbf{J}_{Li}^b = -D_{Li}^b \nabla c_{Li}^b, \quad \mathbf{x} \in \Omega_b, \tag{5}$$

where $D_{Li}{}^b$ is the diffusion coefficient (m^2 s^{-1}) for Li in the buffer.

Equation 5 is subject to the initial condition

$$c_{Li}^b(\mathbf{x}, 0) = 0, \qquad \mathbf{x} \in \Omega_b, \tag{6}$$

and the boundary conditions on $\Gamma(t)$ and Γ_1. In addition to the kinematic condition in Eq. 2, these conditions are

$$\mathbf{n} \cdot \mathbf{J}_{Li}^b = R_\Gamma, \qquad \mathbf{x} \in \Gamma(t), \tag{7}$$

and

$$D_{Li}^b \frac{\partial c_{Li}^b}{\partial x}(L_1, y, t) = R_{Li}, \qquad 0 < y < B. \tag{8}$$

They encode mass conservation across the interfaces bounding the buffer Ω_b. Specifically, Eq. 8 specifies that the normal component of $\mathbf{J}_{Li}^b$ across the buffer/electrolyte interface Γ_1 is proportional to the net reaction rate, R_1, of the Faradaic reaction $Li^+ + e^- \rightarrow Li$; this rate is given by the Butler-Volmer equation,

$$R_{Li} = -\frac{k_0}{\gamma_{ts}}\left[a_R \exp\left(\alpha_{an}\frac{zF\eta_\alpha + 2\omega\gamma_1\kappa}{RT}\right) - a_O a_e^z \exp\left(-\alpha_{cat}\frac{zF\eta_\alpha + 2\omega\gamma_1\kappa}{RT}\right)\right]. \tag{9a}$$

Here, k_0 is the reaction rate constant (mol/m^2/s); R is the universal gas constant (J/mol/K); γ_{ts} is the activity coefficient of the transition state for the Faradaic reaction (−); a_e, a_O and a_R are the activities of electrons and oxidant (e.g., Li^+) and reductant (e.g., Li atom), respectively; α_{an} and α_{cat} are the anodic and cathodic charge-transfer coefficients, respectively (−); γ_1 is the isotropic surface energy at the interface Γ_1 (J m^{-2}); and the activation overpotential η_α is defined as

$$\eta_\alpha = \varphi_e - \varphi_b(L_1, y, t) - E^\Theta, \tag{9b}$$

where E^Θ is the standard electrode potential.[1] Since Γ_1 is a straight line, its curvature is $\kappa = 0$. Finally, $a_R = c_{Li}^b(L_1, y, t)/c^\Theta$, where c^Θ is the standard concentration.

By the same token, Eq. 7 signifies that the normal mass flux of Li atoms across $\Gamma(t)$, $\mathbf{n} \cdot \mathbf{J}_{Li}^b$, is supplied by the Li deposition rate, R_Γ. The latter is driven by the difference in the chemical potentials of Li across the Li-metal/buffer interface, for which we adopt the Butler-Volmer form,

$$R_\Gamma = -\frac{k_\Gamma}{\gamma_{ts}}\left[\exp\left(\alpha_{an}\frac{2\omega\gamma\kappa - zFE^\Theta}{RT}\right) - \frac{c_{Li}^b(\mathbf{x} \in \Gamma, t)}{c^\Theta}\exp\left(-\alpha_{cat}\frac{2\omega\gamma\kappa - zFE^\Theta}{RT}\right)\right], \tag{10}$$

where γ is the isotropic surface energy (J m^{-2}) at the interface Γ. To be specific, we set the reaction rate constant $k_\Gamma = k_0$.

[1] In all numerical experiments reported below, we set $\gamma_{ts} = 1$, $a_e = 1$, $\alpha_{an} = 1 - \alpha_{cat}$, and $E^\Theta = 0$. We also set $a_R = 1$ and $a_O = 1$ in our simulations of ASSBs without a buffer, i.e., when the Li-metal anode and the solid electrolyte are in direct contact.

The boundary value problem comprising Eqs. 1–10 requires the knowledge of $c_{Li}^b(L_1, y, t)$ and $\phi_b(L_1, y, t) \equiv \phi(t)$. These boundary functions are computed from the continuity conditions at the interface Γ_1 separating the buffer and the electrolyte. Thus, the normal component of the current density, $\mathbf{i}_{el} = (i_{el,x}, i_{el,y})^\top$, entering the buffer from the electrolyte at the interface Γ_1 is proportional to the net reaction rate of the Faradaic reaction $Li^+ + e^- \rightarrow Li$:

$$i_{el,x}(L_1, y, t) = zFR_{Li}. \tag{11}$$

That is because, at the flat electrolyte/buffer interface, $J_{Li,x}^b = J_{Li^+,x}^b = R_{Li}$.

Scenario 2: Buffer with low electronic conductivity. Buffers with $\sigma_e \ll \sigma_{Li^+}$ are electronic insulators with high ionic conductivity; examples include i) solid electrolyte materials whose properties differ from those of the solid electrolyte used in a given ASSLB and ii) compositions of the solid electrolyte interface (SEI) formed in an organic liquid electrolyte. Such a buffer, Ω_b, acts as a single-ion conductor with a constant Li^+ concentration $c_{Li^+}^b$.[15,19,20] The ions Li^+ undergo the Faradaic reaction, reducing to Li atoms, on the anode surface $\Gamma(t)$.

The spatial distribution of electric potential $\phi_b(\mathbf{x}, t)$ within the buffer Ω_b is governed by the Laplace equation,

$$\nabla \cdot \mathbf{i}_b = 0, \qquad \mathbf{i}_b = -\sigma_b \nabla \varphi_b, \qquad \mathbf{x} \in \Omega_b, \tag{12}$$

where σ_b is the ionic conductivity for Li^+ in the buffer (S m^{-1}), and $\mathbf{i}_b(\mathbf{x}, t)$ is the current density in the buffer (m^2 s^{-1}). Equation 12 is subject to boundary conditions on $\Gamma(t)$ and Γ_1. On the moving surface $\Gamma(t)$, we supplement the kinematic boundary condition in Eq. 2 with the mass balance relation

$$\mathbf{n} \cdot \mathbf{i}_b = zFR_{Li}, \qquad \mathbf{x} \in \Gamma(t). \tag{13}$$

The production rate of Li atoms, R_{Li}, is now given by

$$R_{Li} = -\frac{k_0}{\gamma_{ts}}\left[\exp\left(\alpha_{an}\frac{zF\eta_\alpha + 2\omega\gamma_{Li}^b\kappa}{RT}\right) - \frac{c_{Li^+}^b}{c^\Theta}\exp\left(-\alpha_{cat}\frac{zF\eta_\alpha + 2\omega\gamma_{Li}^b\kappa}{RT}\right)\right]. \tag{14}$$

The activation overpotential η_α is now defined as $\eta_\alpha = \phi_e - \phi_b(\mathbf{x} \in \Gamma(t), t) - E^\Theta$.

At the buffer/electrolyte interface, Γ_1, we ensure the continuity of electric potential and normal components of the charge flux:

$$\varphi_b(L_1, y) = \varphi_{el}(L_1, y), \qquad \frac{\partial i_{b,x}}{\partial x}(L_1, y) = \frac{\partial i_{el,x}}{\partial x}(L_1, y). \tag{15}$$

In the Butler-Volmer expressions 9, 10 and 14, the surface energy terms $2\omega\gamma_1\kappa/(RT)$, $2\omega\gamma\kappa/(RT)$ and $2\omega\gamma_{Li}^b\kappa/(RT)$ are included to account for the effect of the surface curvature on the reactions' energy barrier.[21] They act to flatten the electrode surface, since the creation of additional surface area results in a surface energy penalty.[14]

Stability Analysis

Linear stability analysis is performed by applying a small perturbation, $\varepsilon \exp(wt + iky)$, to a one-dimensional steady-state base state, defined by the flat electrode surface $h^{(0)}(t) \equiv Ut$ moving with the constant velocity $U = \mathrm{d}h^{(0)}/\mathrm{d}t = -\omega R_{Li}^{(0)}$ and by the corresponding electric potential $\phi^{(0)}(x)$ and Li^+ concentration $c^{(0)}(x)$. (The spatial profiles of $\phi^{(0)}$ are shown in Fig. A·1 in Appendix A). Here, ε is the dimensionless small parameter

($\varepsilon \ll L_1/L \ll 1$), w is the growth rate (1/s), k is the wavenumber (1/m), and $i^2 = -1$. The electrodeposition process is unstable if the perturbations grow with time, i.e., if $w > 0$. The goal of a stability analysis is to express w in terms of the physical properties of the solid electrolyte, buffer and anode.

The mathematical details of this analysis are provided in Appendices A and B. The results are reported below in terms of dimensionless growth rate, wavenumber, and current density,

$$\tilde{w} = \frac{wF^2c_0L^2}{\sigma_{el}RT}, \quad \tilde{k} = kL, \quad \text{and}$$
$$\tilde{I} = \frac{LFI}{zRT\sigma_{el}} = \frac{\tilde{R}_{Li}}{z}. \qquad [16]$$

Results and Discussion

The parameter values used in our stability analysis are presented in Table I. For illustration purposes, we choose lithium lanthanum zirconium oxide ($Li_7La_3Zr_2O_{12}$, LLZO) as the solid electrolyte. To ensure that the standard electrode potential, E^{Θ} is 0 for Scenarios 1 and 2, we define the standard concentration c^{Θ} to be either the Li concentration in the lithium metal, $c^{\Theta} = c_{Li}$, in Scenario 1 or the Li^+ concentration in the solid electrolyte, $c^{\Theta} = c_0$, in Scenario 2.

Figures 2 and 3 exhibit the dispersion relations, $\tilde{w} = \tilde{w}(\tilde{k})$, and the corresponding stability regimes for ASSBs with and without a buffer. Only the results for high-conductivity buffers (Scenario 1) are shown. That is because their counterparts for low-conductivity buffers (Scenario 2) overlap with the solutions in the absence of a buffer when $\sigma_b/\sigma_{el} = 1$, according to Eq. B·8. These results are obtained by solving the boundary-value problems in Appendix A numerically and, under certain approximations, analytically (Appendix B). Figure 2 demonstrates that the numerical and analytical solutions are virtually indistinguishable; thus, the subsequent figures display only analytical results. In Fig. 2, the range of wavenumbers $\tilde{k}$ corresponding to the positive growth rate $\tilde{w}$ identifies the conditions under which the surface growth is unstable and dendrites develop; the maximum value $\tilde{w}_{max} = \tilde{w}(\tilde{k}_{max})$ indicates the regime wherein the electrode surface growth is maximally unstable, while the regime with $\tilde{k}_{cr}$ corresponds to the marginally stable electrode surface. Both $\tilde{w}_{max}$ and $\tilde{k}_{cr}$ increase with the applied potential ϕ_e. When $\tilde{k} > \tilde{k}_{cr}$, the surface is stable because $\tilde{w} < 0$ due to the surface energy penalty on the creation of additional surface area. This penalty is quantified by the terms proportional to capillary numbers for the electrolyte and buffer, Ca^{el}_{Li} and Ca^{b}_{Li}, in Eqs. B·3a and B·6.

In the absence of a buffer, the growth rate $\tilde{w}$ is maximal at $\tilde{k} = 0$ as the electric potential gradient always acts as a destabilization source and no stabilization mechanism is involved (Fig. 2). That is in contrast to the high-conductivity buffer, for which the dispersion relation $\tilde{w} = \tilde{w}(\tilde{k})$ is non-monotonic: $\tilde{w}$ increases from a small positive value at $\tilde{k} = 0$ to its maximum value $\tilde{w}_{max}$, after which it decreases and eventually becomes negative. Diffusion of Li in the buffer has a stabilizing effect by reducing the growth rate $\tilde{w}$ at all wavenumbers $\tilde{k}$. A proper selection of the transport properties of the buffer material ($\tilde{D}_b$ and Ca^{b}_{Li}/Ca^{el}_{Li}) would allow one to reduce both the maximal growth rate $\tilde{w}_{max}$ and the critical wavenumber $\tilde{k}_{cr}$, i.e., to extend the operational range over which the electrodeposition on the Li anode remains stable.

The stability of electrodeposition, encapsulated in the dispersion relation $\tilde{w} = \tilde{w}(\tilde{k})$, depends on both the materials properties and the battery operating conditions (the applied electric potential ϕ_e or the current density I). Figure 3 identifies the stability regimes, $\tilde{w} = \tilde{w}(\tilde{k}; \tilde{I}^{(0)})$ given by Eqs. B·8 and B·3a, for ASSBs without a buffer and with a highly conductive buffer, respectively. Defining the critical wavenumber $\tilde{k}_{cr}$ as the wavenumber at which $w = 0$, yields the curve $\tilde{I}^{(0)} = \tilde{I}^{(0)}(\tilde{k}_{cr})$ that separates the stable ($w < 0$) and unstable ($w > 0$) regimes. The presence of a high-conductivity buffer (with $\tilde{D}_b = 1$ and $Ca^{b}_{Li} = Ca^{el}_{Li}$) significantly expands the stability of electrodeposition at any current density, i.e., the size of the blue region in which $w < 0$. In the absence of a buffer, Li deposition becomes progressively unstable as I increases. The stability diagrams in Fig. 3 provide a blueprint for the electrode-morphology design: they suggest that deploying Li-metal anodes whose surface roughness wavelength λ is smaller than the critical wavelength $\lambda_{cr} = 2\pi/\tilde{k}_{cr}$ would ameliorate dendritic growth. Such surfaces can be manufactured with, e.g., nano-structuring.[27]

Dependence of the dispersion relations $\tilde{w} = \tilde{w}(\tilde{k})$ on the electrochemical characteristics of the electrolyte and buffer suggests the use of these relations as a screening tool for materials selection. To this end, we investigate three metal materials as candidates for a highly conductive buffer: silver (Ag), aluminum (Al) and tin (Sn). Their transport properties (Li diffusivity, electronic conductivity) and interfacial energies at room temperature, $T = 298.15$ K are collated in Table II. The Li-metal/buffer interfacial energies are computed as[33] $\gamma^{b}_{Li} = \gamma_{Li} + \gamma_b - 0.5\sqrt{\gamma_{Li}\gamma_b}$, where γ_{Li} and γ_b are the surface energies of the Li and coating materials reported in Ref. 31. The dimensionless electronic conductivity $\tilde{\sigma}_e$ of these metals is at least seven orders of magnitude larger than the dimensionless Li diffusivity, $\tilde{D}_b$. Thus, the assumption of high and constant electron concentration in the buffer is valid, and the Faradaic reaction

Table I. Model parameters used in the stability analysis.

Parameter	Value	References
Half-cell length, L (μm)	10	22
Buffer layer thickness, L_1 (nm)	20	
Ionic conductivity for Li^+ in solid electrolyte, σ_{el} (S m^{-1})	0.1	23
Temperature, T (K)	298.15	
Molecular weight of lithium metal, M (g mol^{-1})	6.941	24
Density of lithium metal, ρ (g cm^{-3})	0.534	24
Li concentration in lithium metal, c_{Li} (mol m^{-3})	76,934	24
Concentration of Li^+ in solid electrolyte, c_0 (mol m^{-3})	18,012	3
Standard concentration, c^{Θ} (mol m^{-3})	c_{Li}, c_0	
Standard electrode potential, E^{Θ} (V)	0	
Reaction rate constant, k_0 (mol/(m^2s))	$1 \cdot 10^{-2}$	25
Surface energy of Li/LLZO interface, $\gamma_{Li/el}$ (J m^{-2})	0.85	26
Activity coefficient of the transition state, γ_{ts} (—)	1	

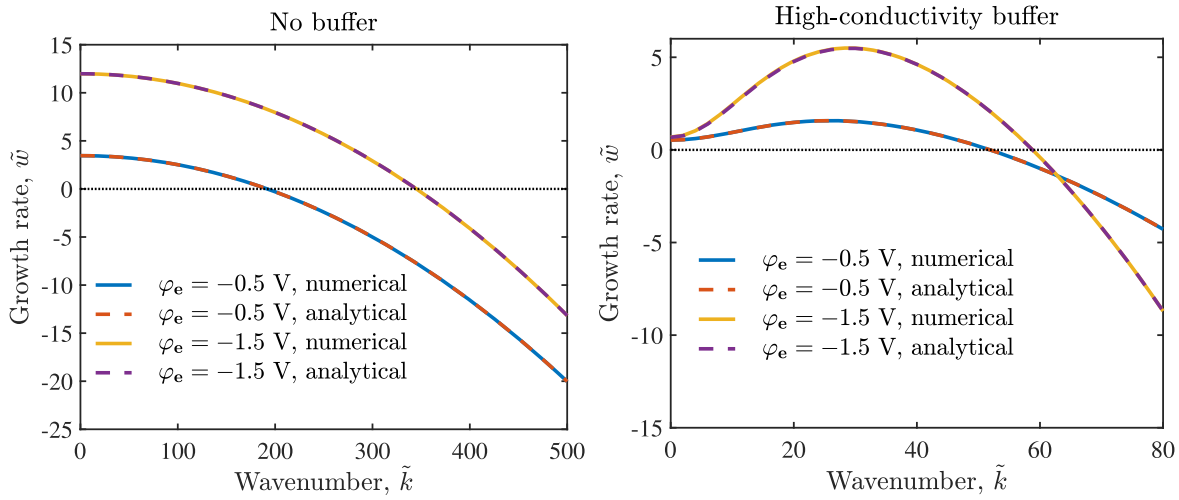

Figure 2. Dispersion relations $\tilde{w} = \tilde{w}(\tilde{k})$ for ASSBs without a buffer and with the high-conductivity buffer ($\tilde{D}_b = 1$ and $Ca^{el}_{Li} = Ca^{b}_{Li}$), for $\phi_e = -0.5$ V and -1.5 V. The solid and dashed lines are the numerical and analytical solutions, respectively.

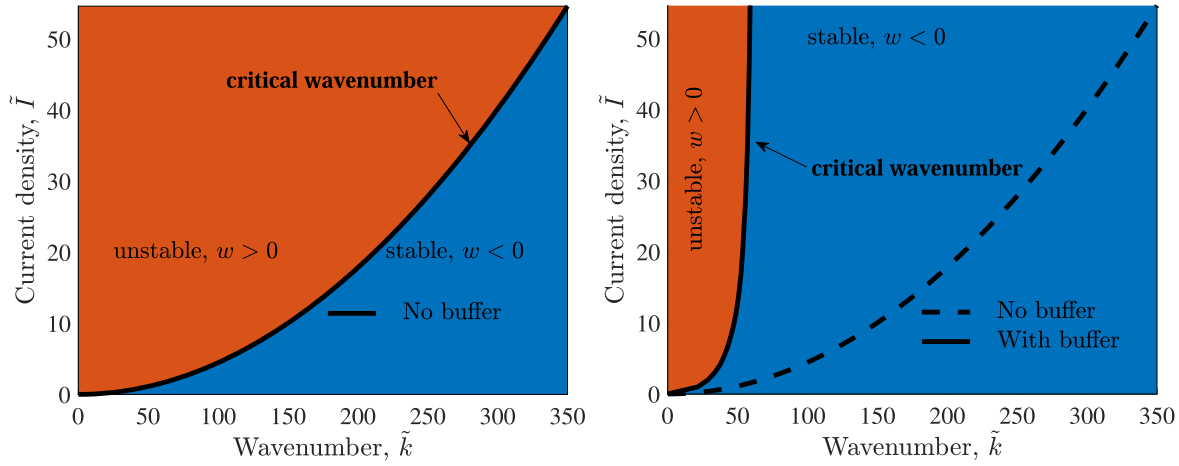

Figure 3. Stability regimes predicted by Eqs. B·8 and B·3a for ASSBs without a buffer (Left) and with a high-conductivity buffer ($\tilde{D}_b = 1$ and $Ca^{b}_{Li} = Ca^{el}_{Li}$) (Right). The solid/dashed lines denote the critical wavenumber $\tilde{k}_{cr}$ for each current density $\tilde{I}^{(0)}$; these lines, along which $w = 0$, separate the stable ($w < 0$, blue) and unstable ($w > 0$, red) regions.

Table II. Transport properties and interfacial energies for buffer materials with high electronic conductivity at room temperature, T = 298.15 K.

	Ag		Al		Sn	
Property	Value	References	Value	References	Value	References
Li diffusion coefficient, D_b ($m^2\ s^{-1}$)	$1 \cdot 10^{-10}$	28	$8.43 \cdot 10^{-12}$	29	$4.15 \cdot 10^{-12}$	30
Dimensionless Li diffusivity, $\tilde{D}_b$	67.64		5.71		2.81	
Interfacial energy, γ^{b}_{Li} ($J\ m^{-2}$)	1.36	31	1.28	31	0.93	31
Ratio Ca^{b}_{Li}/Ca^{el}_{Li}	1.6		1.5		1.1	
Electronic conductivity, σ_e ($S\ m^{-1}$)	$6.67 \cdot 10^{7}$	32	$4.08 \cdot 10^{7}$	32	$8.7 \cdot 10^{6}$	32
Dimensionless e^- conductivity, $\tilde{\sigma}_e$	$6.67 \cdot 10^{8}$		$4.08 \cdot 10^{8}$		$8.7 \cdot 10^{7}$	

$Li^+ + e^- \rightarrow Li$ takes place at the buffer/electrolyte interface. The dispersion relations $\tilde{w} = \tilde{w}(\tilde{k})$ for Ag, Al and Sn buffers at $\phi_e = -1.5$ V are shown in Fig. 4. The use of Ag as a buffer material yields the negative growth rate $\tilde{w}$ for wavenumber $\tilde{k}$ that is slightly larger than 0. For Al and Sn buffers, $\tilde{w}$ is positive for small $\tilde{k}$ and negative for a wide range of $\tilde{k} > \tilde{k}_{cr}$. All three buffer materials dramatically expand the stable regime relative to that of an ASSB without a buffer. Our results confirm the experimental findings[6,7] according to which the use of Ag buffers mitigates dendritic growth because the dimensionless diffusivity of Li in Ag is larger than the dimensionless Li^+ conductivity in the solid electrolyte. Another reason is that the interfacial energy between Ag and Li-metal is higher than that between the solid electrolyte and Li-metal. While somewhat less efficient in dendrite suppression, Al and Sn are plausible buffer materials, especially considering their lower cost.

Next, we apply our analysis to buffer materials with low electronic conductivity, specifically, two antiperovskite super ionic conductors, $Li_{2.99}Ba_{0.005}OCl$[12] and $Li_3S(BF_4)_{0.5}Cl_{0.5}$.[13] Table III

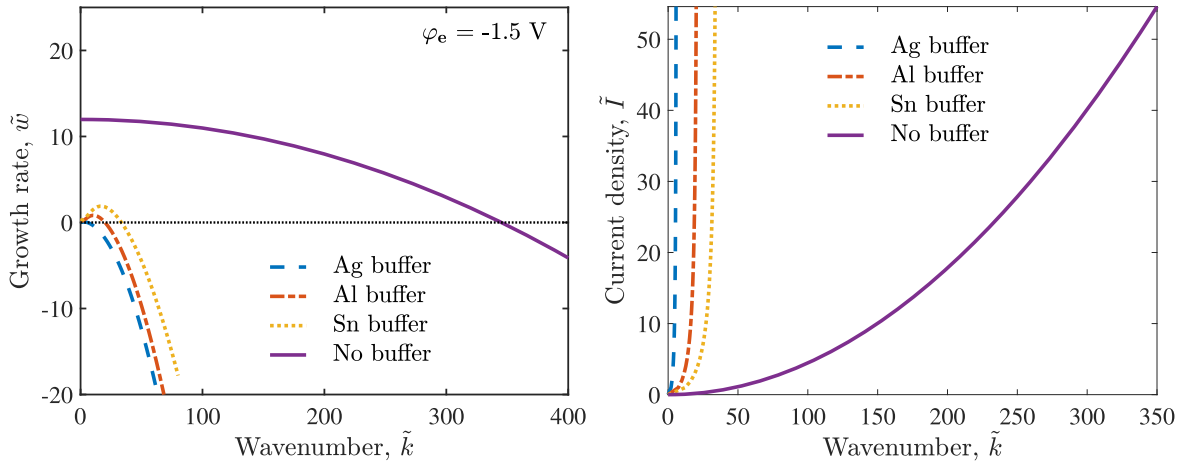

Figure 4. Dispersion relations $\tilde{w} = \tilde{w}(\tilde{k})$ at $\phi_e = -1.5$ V (Left) and stability regimes $\tilde{w} = \tilde{w}(\tilde{k}; \tilde{I}^{(0)})$ (Right), for ASSBs without a buffer and with Ag, Al and Sn buffers. The lines in the right graph, along which $w = 0$ and $\tilde{k} = \tilde{k}_{cr}$, separate the stable ($w < 0$) and unstable ($w > 0$) regions.

Table III. Transport properties and interfacial energies for coating materials with low electronic conductivity at room temperature, T = 298.15 K.

	$Li_3S(BF_4)_{0.5}Cl_{0.5}$		$Li_{2.99}Ba_{0.005}OCl$	
Property	Value	References	Value	References
Ionic conductivity for Li^+, σ_b (S m^{-1})	10	13	1	12
Dimensionless Li^+ conductivity, $\tilde{\sigma}_b$	100		10	
Li^+ concentration, $c_{Li}{}^b$ (mol m^{-3})	26,629	13	93,531	12
Dimensionless Li^+ concentration, $\tilde{c}_{Li}^b$	1.45		5.19	
Interfacial energy, γ_b^{Li} (J m^{-2})	0.65	34	0.65	34
Ratio Ca_{Li}^b/Ca_{Li}^{el}	0.76		0.76	
Electronic conductivity, σ_e (S m^{-1})	negligible	13	negligible	12

reports their ionic conductivity and interfacial energy at room temperature, $T = 298.15$ K; in the absence of the interfacial energies for electrolyte/buffer systems, we use the interfacial energy of an antiperovskite super ionic conductor, Li_3OCl.[34] For both materials, the dimensionless electronic conductivity $\tilde{\sigma}_e$ is many orders of magnitude smaller than the dimensionless Li^+ conductivity and, thus, Li^+ ions undergo the Faradaic reaction with e^- and reduce to Li atoms at the anode/buffer interface, $x = L_1$. Figure 5 suggests that buffers made of materials with low electronic conductivity and ionic conductivity for Li^+ higher than that in the solid electrolyte (LLZO), such as the antiperovskite super ionic conductors, $Li_3S(BF_4)_{0.5}Cl_{0.5}$ and $Li_{2.99}Ba_{0.005}OCl$, suppress dendrite growth.

One might expect the buffer thickness, L_1, to affect the buffer's ability to suppress dendrite growth and, thus, to act as another design variable. According to Eqs. B·4 and B·7, at any given current density $I^{(0)}$, the critical wavenumber k_{cr} is independent of L_1, regardless of whether the buffer has high or low electronic conductivity. However, L_1 does impact the maximum growth rate w_{max}, with the nonlinear dependence of the growth rate on the buffer thickness, $w = w(L_1)$, given by Eq. B·3a for buffers with high electronic conductivity and

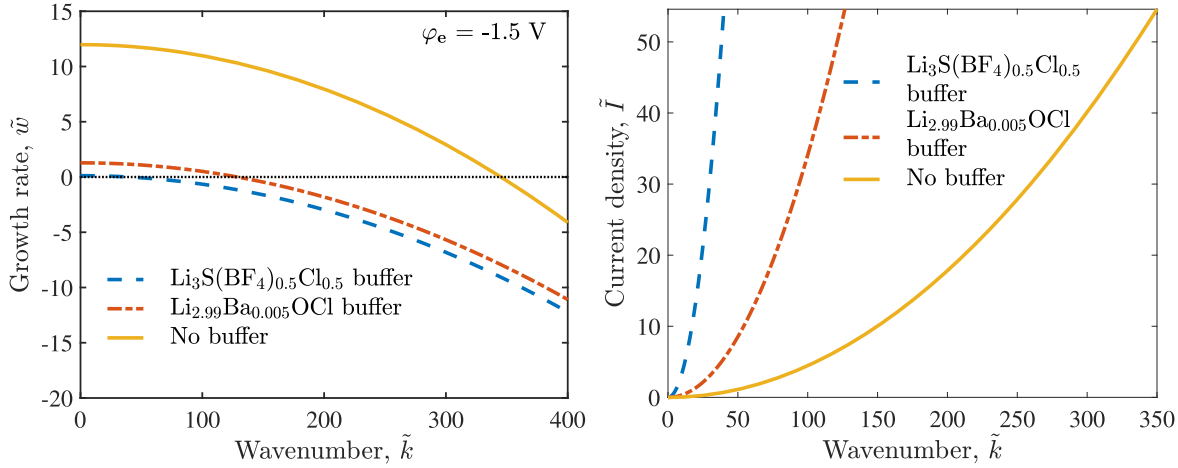

Figure 5. Dispersion relations $\tilde{w} = \tilde{w}(\tilde{k})$ at $\phi_e = -1.5$ V (Left) and stability regimes $\tilde{w} = \tilde{w}(\tilde{k}; \tilde{I}^{(0)})$ (Right), for ASSBs without a buffer and with the $Li_3S(BF_4)_{0.5}Cl_{0.5}$ and $Li_{2.99}Ba_{0.005}OCl$ buffers. The lines in the right graph, along which $w = 0$ and $\tilde{k} = \tilde{k}_{cr}$, separate the stable ($w < 0$) and unstable ($w > 0$) regions.

by Eq. B·6 for low-conductivity buffers. These equations point to the complex interplay between the buffer's size and transport properties. For example, according to Eq. B·6, w decreases or increases with L_1 depending on whether $\sigma_b > \sigma_{el}$ or $\sigma_b < \sigma_{el}$.

Finally, we validate our analysis by comparing its predictions with the previously published experiments. This task proved to be challenging because many experimental studies do not report all the relevant material properties and even fewer studies report negative results. With these caveats, all the experimental results we are aware of conform to our stability diagrams (Fig. 6). For buffer materials with high electronic conductivity and positive interfacial energies, $\gamma_{Li}^{el} > 0$ and $\gamma_{Li}^{b} > 0$, the stability diagram is presented in the $(Ca_{Li}^{b}\tilde{D}_b/Ca_{Li}^{el}, \tilde{I})$ phase space. For low-conductivity buffers with $\gamma_{Li}^{el} > 0$ and $\gamma_{Li}^{b} > 0$, the phase space is spanned by the material properties $\tilde{\sigma}_b$ and Ca_{Li}^{b}/Ca_{Li}^{el}. In both cases, the solid line represents critical wavenumbers $\tilde{k}_{cr}$ for ASSBs without a buffer, such that the insertion of a buffer with given material properties is predicted to have either destabilizing (red region to the left of the solid line) or stabilizing (blue region to the right of the solid line) effect on the Li dendrites. Using the same material properties and operating conditions as in the experiments,[6,35–37] our model confirms that high-conductivity buffers made of Ag, Al, Sn or magnesium (Mg) suppress dendrite growth. For buffers with low electronic conductivity, our model predictions are consistent with the experimental results[38,39] that Al_2O_3 and Li_3N stabilize the electrodeposition on the Li anode, while lithium carbonate (Li_2CO_3) fails to suppress dendrite growth due to its relatively low ionic conductivity and interfacial energy with Li-metal.

The stability diagrams in Fig. 6 do not include buffers and solid electrolytes that have negative interfacial energies with Li-metal, $\gamma_{Li}^{el} < 0$ and/or $\gamma_{Li}^{b} < 0$. That is because, according to our predictions based on Eqs. B·3a and B·6, negative values of the capillary numbers Ca_{Li}^{el} or Ca_{Li}^{b} always yield positive growth rate w, which signifies that the electrode surface growth is unconditionally unstable. This conclusion is in line with the experimental study,[40] which found $\gamma_{Li}^{el} < 0$ to indicate an intrinsically unstable interface between the solid electrolyte (e.g., LPS) and the Li-metal, and suggested the potential dendrite suppression abilities of buffer materials with $\gamma_{Li}^{el} > 0$.

Conclusions

The insertion of a buffer layer between the Li-metal anode and the solid (ceramic) electrolyte has been proposed as a possible strategy to suppress Li dendrite formation in ASSBs. We investigated this possibility by presenting a mathematical model of electrodeposition on the Li anode of ASSBs with and without such a buffer layer, with focus on the stability of the evolving anode surface in response to a small perturbation. Our key result is analytical expressions that relate the instability growth-rate to both material properties (transport properties of the electrolyte and buffer and interfacial energy) and battery operating conditions (current density or applied electric potential). Our analysis leads to the following major conclusions.

- Our stability diagrams correctly identify buffer materials that are experimentally shown to suppress/mitigate dendrite growth in ASSBs. These materials can have either high (e.g., Ag, Al, Sn, Mg) or low (e.g., Al_2O_3 and Li_3N) electronic conductivity, provided they have positive interfacial energy.
- Our analysis correctly identifies buffer materials that, in experiments, failed to impact dendrite growth. These materials have either low ionic conductivity and interfacial energy with Li-metal (e.g., Li_2CO_3) or have negative interfacial energy with Li-metal (e.g., LPS).
- Our stability diagrams suggest that prospective buffer materials should have either high electronic conductivity and high Li diffusion coefficient or low electronic conductivity and high ionic conductivity for Li^+; materials with high interfacial energy with Li-metal are preferred.
- Candidates for buffer materials with low electronic conductivity include antiperovskite super ionic conductors, $Li_{2.99}Ba_{0.005}OCl$ and $Li_3S(BF_4)_{0.5}Cl_{0.5}$, because their Li diffusivity is higher than that of most currently proposed solid electrolytes.
- Our analysis demonstrates that the buffer thickness has no impact on the critical surface roughness wavelength, below which the interface is stable and no dendrites initiate.

Our findings suggest new strategies for the design of interfacial buffers, i.e., for the optimal selection of buffer material and the solid electrolyte pair based on their electrochemical and physical properties. Our model enables a quantitative evaluation of the buffer materials and, when combined with experimental and computational

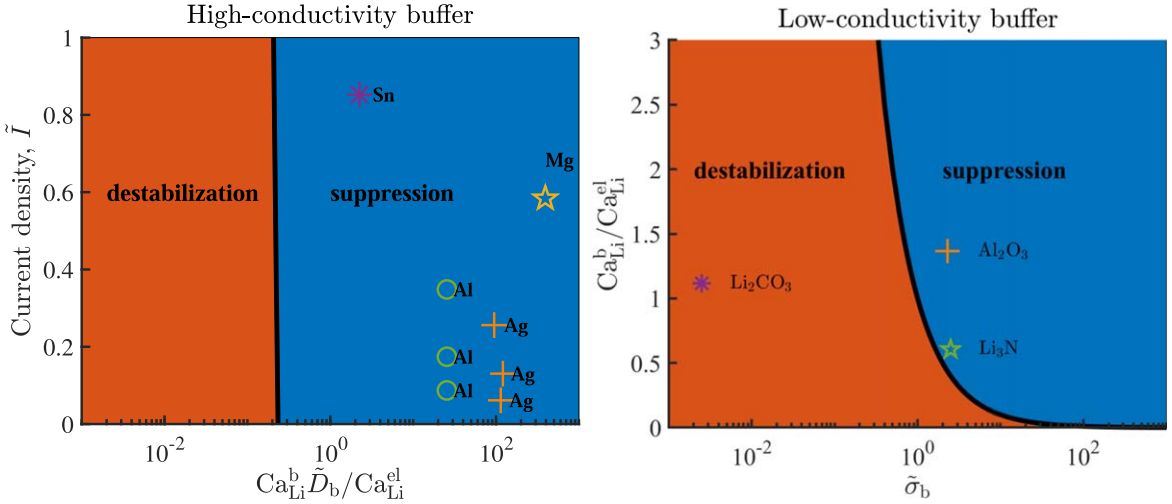

Figure 6. Stability diagrams in the phase space spanned by dimensionless parameters $(Ca_{Li}^{b}\tilde{D}_b/Ca_{Li}^{el}, \tilde{I})$ and $(\tilde{\sigma}_b, Ca_{Li}^{b}/Ca_{Li}^{el})$ for buffer materials with high and low electronic conductivity, respectively. In both cases, the interfacial energies are positive, $\gamma_{Li}^{el} > 0$ and $\gamma_{Li}^{b} > 0$. The solid line represents critical wavenumbers $\tilde{k}_{cr}$ for ASSBs without a buffer, such that the insertion of a buffer with given material properties is predicted to have either destabilizing (red region to the left of the solid line) or stabilizing (blue region to the right of the solid line) effect on the Li dendrites. The experimental data for Ag, Al, Sn, Mg, Al_2O_3, Li_3N, and Li_2CO_3 are from Refs. 6, 35–39.

approaches that provide improved characterization of the material properties, would accelerate the discovery of new buffer materials.

In future work, we will extend our model to handle buffer materials with intermediate electronic and ionic conductivities and couple ion transport and mechanical behaviors in ASSBs. We will also investigate the effects of operating conditions and aging on dendrite suppression by changing the ionic conductivity and Li concentration in the solid electrolyte or buffer materials.

Finally, our analysis points to the possibility of using Li-metal anodes with randomly rough surfaces as a means to suppress or mitigate dendrite initiation. Such a strategy has proved to be beneficial in other applications, e.g., Ref. 41; its mathematical treatment would necessitate the adoption of a probabilistic framework.[42,43]

Acknowledgments

We thank Prof. Yiguang Ju, Princeton University, for bringing this problem to our attention and Dr. Xin Xu, Stanford University, for many useful discussions. This work was supported in part by Air Force Office of Scientific Research under award number FA9550-21-1-0381, by Hyundai Motor Group, and by StorageX at Stanford University.

Appendix A. Perturbation Analysis

We introduce dimensionless variables

$$\tilde{x} = \frac{x}{L}, \quad \tilde{y} = \frac{y}{L}, \quad \tilde{t} = \frac{t\sigma_{\rm el}RT}{F^2c_0L^2}, \quad \tilde{c} = \frac{c}{c_0},$$
$$\tilde{\varphi} = \frac{F\varphi}{RT}, \quad \tilde{h} = \frac{h}{L}, \quad \tilde{\kappa} = L\kappa \qquad [A\cdot1a]$$

and model parameters

$$\tilde{\sigma} = \frac{\sigma}{\sigma_{\rm el}}, \quad \tilde{D}_{\rm b} = \frac{D_{\rm b}F^2c_0}{\sigma_{\rm el}RT}, \quad \tilde{c}^{\Theta} = \frac{c^{\Theta}}{c_0},$$
$$\tilde{k}_0 = \frac{LF^2k_0}{RT\sigma_{\rm el}\gamma_{\rm ts}}, \quad \tilde{\eta}_{\alpha} = \frac{F\eta_{\alpha}}{RT}. \qquad [A\cdot1b]$$

We also define the capillary numbers

$$\mathrm{Ca}^{\rm el}_{\rm Li} = \frac{\omega\gamma^{\rm el}_{\rm Li}}{RTL}, \quad \mathrm{Ca}^{\rm b}_{\rm Li} = \frac{\omega\gamma^{\rm b}_{\rm Li}}{RTL} \qquad [A\cdot1c]$$

and the normalized rate of Li production $\tilde{R}_{\rm Li}$ and the interfacial current density $\tilde{I}$ as

$$\tilde{R}_{\rm Li} = \frac{LF^2R_{\rm Li}}{RT\sigma_{\rm el}}, \quad \tilde{I} = \frac{LFI}{zRT\sigma_{\rm el}} = \frac{\tilde{R}_{\rm Li}}{z}. \qquad [A\cdot1d]$$

Unless specified otherwise, all the quantities below are dimensionless, even though we drop the tildes to simplify the notation.

The electrode surface height, $h(y, t)$, and the state variables $\phi(\mathbf{x}, t)$ and $c(\mathbf{x}, t)$ are written as

$$h = h^{(0)}(t) + \hat{\varepsilon}h^{(1)}, \quad \varphi = \varphi^{(0)}(x) + \hat{\varepsilon}\varphi^{(1)},$$
$$c = c^{(0)}(x) + \hat{\varepsilon}c^{(1)}, \quad \hat{\varepsilon} = \varepsilon e^{wt+iky}, \qquad [A\cdot2]$$

where the constant $h^{(1)}$ and the functions $\phi^{(1)}(x)$ and $c^{(1)}(x)$ are first-order (in ε) corrections to the base state denoted by the superscript $^{(0)}$.

The evolving electrode surface $\Gamma(t)$, which consists of points $(y, h(y, t))^{\top}$, is a perturbation around the base state $\Gamma^{(0)} = \{\mathbf{x} = (x, y)^{\top}: x = h^{(0)}, 0 \leqslant y \leqslant B/L\}$. It follows from Eq. 1 that first-order approximations of its unit normal vector, $\mathbf{n} = \mathbf{n}^{(0)} + \mathcal{O}(\varepsilon^2)$, and curvature, $\kappa = \kappa^{(0)} + \hat{\varepsilon}\kappa^{(1)}$, are given by

$$\mathbf{n}^{(0)} = \begin{pmatrix} -1 \\ 0 \end{pmatrix}, \qquad \kappa^{(0)} = 0, \qquad \kappa^{(1)} = \frac{k^2}{2}h^{(1)}. \qquad [A\cdot3]$$

It follows from Eq. 2 that the interface $h^{(0)}(t)$ is moving with velocity $U = \mathrm{d}h^{(0)}/\mathrm{d}t$. Depending on the buffer type, this velocity is given by either $U = -\omega R^{(0)}_{\Gamma}$ (Eq. 7, Scenario 1) or $U = -\omega R^{(0)}_{\rm Li}$ (Eq. 13, Scenario 2).

In this formulation, the buffer is represented by the domain $\tilde{\Omega}^{(0)}_{\rm b} = \{\tilde{x} : \tilde{h}^{(0)}(t) < \tilde{x} < \tilde{L}_{\rm l}\}$ and the solid electrolyte by the domain $\tilde{\Omega}^{(0)}_{\rm el} = \{\tilde{x}: \tilde{L}_{\rm l} < \tilde{x} < 1\}$, where $\tilde{L}_{\rm l} = L_{\rm l}/L$. As mentioned above, we drop the tilde to simplify the notation.

A.1. Solid electrolyte.—Substituting Eq. A·2 into the dimensionless form of Eqs. 3 and 4, and collecting the terms of order ε^0 and ε leads to the PDEs for $\varphi^{(n)}_{\rm el}(x)$,

$$\frac{\mathrm{d}i^{(n)}_{\rm el}}{\mathrm{d}x} = 0, \quad i^{(n)}_{\rm el} = -\sigma_{\rm el}\frac{\mathrm{d}\varphi^{(i)}_{\rm el}}{\mathrm{d}x},$$
$$n = 0,\ 1, \quad L_1 < x < 1, \qquad [A\cdot4]$$

where $i_{\rm el} = |\mathbf{i}_{\rm el}|$ and $\mathbf{i}^{(n)}_{\rm el} = (i^{(n)}_{\rm el}, 0)^{\top}$ for $n = 0{,}1$. These two equations are subject to the boundary conditions $\varphi^{(n)}_{\rm el}(1) = 0$ and the continuity conditions at the electrolyte/buffer interface $x = L_1$. Integrating these equations once yields

$$i^{(n)}_{\rm el} = -\sigma_{\rm el}\frac{\mathrm{d}\varphi^{(i)}_{\rm el}}{\mathrm{d}x} = a_n, \quad \varphi^{(n)}_{\rm el}(1) = 0, \quad n = 0,\ 1. \qquad [A\cdot5]$$

The constants of integration a_0 and a_1 are determined from the interfacial conditions at $x = L_1$. These conditions depend on the type of buffer material. In Scenario 1, this condition follows from Eqs. 11 and A·1d,

$$i^{(n)}_{\rm el}(L_1) = I^{(n)}_{\rm Li}, \qquad n = 0,\ 1, \qquad [A\cdot6]$$

which specifies these constants as $a_n = I^{(n)}_{\rm Li}$ for $n = 0{,}1$. In Scenario 2, this condition is provided by Eq. 15,

$$\varphi^{(n)}_{\rm el}(L_1) = \varphi^{(n)}_{\rm b}(L_1), \qquad n = 0,\ 1. \qquad [A\cdot7]$$

In accordance with Eq. 14, the interfacial current density depends on the electric potential in the buffer, $I_{\rm Li} = I_{\rm Li}(\phi_{\rm b})$. Hence, in either scenario, the electric potentials in the electrolyte and the buffer are coupled in any approximation order n.

A.2. Scenario 1: High-conductivity buffer.—Substituting Eq. A·2 into the dimensionless form of Eqs. 5–8, and collecting the terms of order ε^0 and ε leads to the BVPs for $c^{(n)}(x)$ used in the approximation of the Li concentration in the buffer, $c^{\rm b}_{\rm Li}(\mathbf{x}, t) \approx c^{(0)}(x) + \hat{\varepsilon}(y, t)c^{(1)}(x)$:

$$J^{(n)} = -D_{\rm b}\frac{\mathrm{d}c^{(n)}}{\mathrm{d}x},$$
$$\frac{\mathrm{d}^2c^{(n)}}{\mathrm{d}x^2} = \begin{cases} 0 & n = 0 \\ (w/D_{\rm b} + k^2)c^{(1)} & n = 1 \end{cases},$$
$$h^{(0)} < x < L_1, \qquad [A\cdot8]$$

subject to the boundary conditions A·6 and

$$-J^{(n)} = R^{(n)}_{\Gamma} \quad \text{at } x = h^{(0)},$$
$$-J^{(n)} = R^{(n)}_{\rm Li} \quad \text{at } x = L_1. \qquad [A\cdot9]$$

In these BVPs, according to Eqs. 9 and 10,

$$R_\Gamma^{(n)} = -k_0 \mathrm{e}^{-\alpha_{\mathrm{cat}} z\eta_\alpha^{(0)}} \begin{cases} \dfrac{c^{(0)}}{c^\Theta}\mathrm{e}^{z\eta_\alpha^{(0)}} - 1 & n = 0 \\ \dfrac{c^{(1)}}{c^\Theta}\mathrm{e}^{z\eta_\alpha^{(0)}} & n = 1 \end{cases} \quad [A\cdot10]$$

and

$$R_{\mathrm{Li}}^{(n)} = k_0 \begin{cases} \dfrac{c^{(0)}}{c^\Theta} - 1 & n = 0 \\ k^2(1 - \alpha_{\mathrm{cat}} + \dfrac{c^{(0)}}{c^\Theta}\alpha_{\mathrm{cat}})h^{(1)}\mathrm{Ca}_{\mathrm{Li}}^{\mathrm{b}} - h^{(1)}\dfrac{\hat{c}^{(1)}}{c^\Theta} & n = 1, \end{cases} \quad [A\cdot11]$$

where $\eta_\alpha^{(0)} = \varphi_{\mathrm{e}} - \varphi_{\mathrm{b}}^{(0)} - E^\Theta$. It follows from Eqs. 2, A·2 and A·3 that

$$wh^{(1)} = \omega c_0 R_{\mathrm{Li}}^{(1)} \quad \text{and} \quad \hat{c}^{(1)} = h^{(1)}\frac{\mathrm{d}c^{(0)}}{\mathrm{d}x} + c^{(1)}. \quad [A\cdot12]$$

The derivation of the boundary condition on the evolving electrode surface $\Gamma(t)$, whose points are represented as $(y, h(y, t))^\top$, requires us to expand $c_{\mathrm{Li}}^{\mathrm{b}}(\mathbf{x} \in \Gamma, t)$ and its gradient in Taylor series around the base state $\Gamma^{(0)} = \{\mathbf{x} = (x, y)^\top : x = h^{(0)}, 0 \leqslant y \leqslant B/L\}$ such that

$$c_{\mathrm{Li}}^{\mathrm{b}}(\mathbf{x} \in \Gamma, t) \approx c^{(0)}(h^{(0)}) + \hat{\varepsilon}\hat{c}^{(1)}(h^{(0)}) \quad [A\cdot13a]$$

and

$$\nabla c_{\mathrm{Li}}^{\mathrm{b}} \approx \mathbf{e}_x\left[\frac{\mathrm{d}c^{(0)}}{\mathrm{d}x}(h^{(0)}) + \hat{\varepsilon}\left(h^{(1)}\frac{\mathrm{d}^2c^{(0)}}{\mathrm{d}x^2} + \frac{\mathrm{d}c^{(1)}}{\mathrm{d}x}\right)_{x=h^{(0)}}\right] + \mathbf{e}_y\hat{\varepsilon}ikc^{(1)}(h^{(0)}). \quad [A\cdot13b]$$

A.3. Scenario 2: Low-conductivity buffer.—Substituting Eq. A·2 into the dimensionless form of Eqs. 12–14, and collecting the terms of order ε^0 and ε leads to the BVPs for $\varphi_{\mathrm{b}}^{(n)}(x)$:

$$i_{\mathrm{b}}^{(n)} = -\sigma_{\mathrm{b}}\frac{\mathrm{d}\varphi_{\mathrm{b}}^{(n)}}{\mathrm{d}x}, \qquad \frac{\mathrm{d}i_{\mathrm{b}}^{(n)}}{\mathrm{d}x} = 0, \quad n = 0, 1; \qquad h^{(0)} < x < L_1, \quad [A\cdot14]$$

subject to boundary conditions A·7 and

$$-i_{\mathrm{b}}^{(n)}(h^{(0)}) = R_{\mathrm{Li}}^{(n)}(h^{(0)}), \qquad i_{\mathrm{b}}^{(n)}(L_1) = i_{\mathrm{el}}^{(n)}(L_1), \quad n = 0, 1. \quad [A\cdot15]$$

Here, $wh^{(1)} = \omega c_0 R_{\mathrm{Li}}^{(1)}$ and

$$R_{\mathrm{Li}}^{(n)} = -k_0 \mathrm{e}^{-\alpha_{\mathrm{cat}} z\eta_\alpha^{(0)}} \times \begin{cases} \mathrm{e}^{z\eta_\alpha^{(0)}} - \frac{c_{\mathrm{Li}}^{\mathrm{b}}}{c^\Theta} & n = 0 \\ \left[(1 - \alpha_{\mathrm{cat}})\mathrm{e}^{z\eta_\alpha^{(0)}} + \alpha_{\mathrm{cat}}\frac{c_{\mathrm{Li}}^{\mathrm{b}}}{c^\Theta}\right](k^2\mathrm{Ca}_{\mathrm{Li}}^{\mathrm{b}}h^{(1)} - z\hat{\varphi}_{\mathrm{b}}^{(1)}) & n = 1. \end{cases} \quad [A\cdot16]$$

The above expression is obtained, similarly to Eq. A·13a, by expanding $\phi_{\mathrm{b}}(\mathbf{x} \in \Gamma, t)$ and its gradient in Taylor series around the base state $\Gamma^{(0)}$, and by defining $\hat{\varphi}_{\mathrm{b}}^{(1)}$ as

$$\hat{\varphi}_{\mathrm{b}}^{(1)} = h^{(1)}\frac{\mathrm{d}\varphi_{\mathrm{b}}^{(0)}}{\mathrm{d}x} + \varphi_{\mathrm{b}}^{(1)}. \quad [A\cdot17]$$

A.4. Battery without a buffer.—The linear stability analysis of ASSBs without a buffer is identical to Scenario 2, in which the transport properties of the buffer are equal to those in the solid electrolyte and the interface $x = L_1$ is absent. Thus, Eqs. A·4–A·7 are replaced with Eq. A·4 defined for the whole domain $h^{(0)} < x < 1$, on which Eqs. A·14–A·17 (minus the interfacial condition at $x = L_1$ and with $\mathrm{Ca}_{\mathrm{Li}}^{\mathrm{b}} = \mathrm{Ca}_{\mathrm{Li}}^{\mathrm{el}}$) are also defined.

A.5. Base-state solutions.—Analytical solutions of the base-state BVPs, i.e., Eqs. A·4–A·16 for $n = 0$, yields the spatial distribution of the electric potential throughout the half cell in Scenario 1,

$$\varphi^{(0)}(\xi; t) = \begin{cases} \varphi_{\mathrm{e}} & 0 \leqslant \xi \leqslant \hat{L}_1 \\ \dfrac{\xi - 1 + Ut}{\sigma_{\mathrm{el}}}R_\Gamma^{(0)} & \hat{L}_1 \leqslant \xi \leqslant 1 \end{cases} \quad [A\cdot18]$$

and in Scenario 2,

$$\varphi^{(0)}(\xi; t) = \begin{cases} \left(\dfrac{\xi - \hat{L}_1}{\sigma_{\mathrm{b}}} + \dfrac{\hat{L}_1 - 1 + Ut}{\sigma_{\mathrm{el}}}\right)R_{\mathrm{Li}}^{(0)} & 0 \leqslant \xi \leqslant \hat{L}_1 \\ \dfrac{\xi - 1 + Ut}{\sigma_{\mathrm{el}}}R_{\mathrm{Li}}^{(0)} & \hat{L}_1 \leqslant \xi \leqslant 1 - Ut. \end{cases} \quad [A\cdot19]$$

These solutions are written in the moving coordinate system $\xi = x - Ut$, with $\hat{L}_1 = L_1 - Ut$. The linear stability analysis is valid for early stages of the dendrite formation, during which $Ut \ll L_1$ and (since $L_1 \ll 1$) $Ut \ll 1$. For these early times, $\phi^{(0)}(\xi; t)$ in Eqs A·18 and A·19 loose their explicit dependence on t, reducing to

$$\varphi^{(0)}(\xi) = \begin{cases} \varphi_{\mathrm{e}} & 0 \leqslant \xi \leqslant L_1 \\ \dfrac{\xi - 1}{\sigma_{\mathrm{el}}}R_\Gamma^{(0)} & L_1 \leqslant \xi \leqslant 1 \end{cases} \quad [A\cdot20]$$

in Scenario 1 and to

$$\varphi^{(0)}(\xi) = \begin{cases} \left(\dfrac{\xi - L_1}{\sigma_{\mathrm{b}}} + \dfrac{L_1 - 1}{\sigma_{\mathrm{el}}}\right)R_{\mathrm{Li}}^{(0)} & 0 \leqslant \xi \leqslant L_1 \\ \dfrac{\xi - 1}{\sigma_{\mathrm{el}}}R_{\mathrm{Li}}^{(0)} & L_1 \leqslant \xi \leqslant 1 \end{cases} \quad [A\cdot21]$$

in Scenario 2.

These solutions are implicit because of the nonlinear dependence of $R_{\mathrm{Li}}^{(0)}$ and $R_\Gamma^{(0)}$ on $\phi^{(0)}(\xi)$ and, in Scenario 1, on

$$c^{(0)}(\xi) = \begin{cases} \dfrac{R_\Gamma^{(0)}}{D_{\mathrm{b}}}\xi + \left(\dfrac{R_\Gamma^{(0)}}{k_0} + 1\right)c^\Theta, & 0 \leqslant \xi \leqslant L_1 \\ 1 & L_1 \leqslant \xi \leqslant 1. \end{cases} \quad [A\cdot22]$$

In other words, for any given ϕ_{e}, these solutions take the form $\varphi^{(0)}(\xi) = \mathcal{F}[\varphi^{(0)}(\xi)]$, where the functional $\mathcal{F}[\cdot]$ is defined by either Eq. A·20 or Eq. A·21. This root-finding problem is solved numerically with the Matlab function `fzero`.

Figure A·1 exhibits the spatial distribution of the base-state electric potential, $\phi^{(0)}(\xi)$, in ASSBs without a buffer and with the highly conductive buffer (Scenario 1 with $D_{\mathrm{b}} = 1$ and $\tilde{\mathrm{Ca}} = 1$). We do not show the solutions for the low-conductivity buffer because they overlap with the buffer-free expressions when $\sigma_{\mathrm{b}} = 1$. The electric potential increases linearly with distance from the evolving anode, ξ, with higher values of the applied potential ϕ_{e} inducing larger potential gradients in the electrolyte. In Scenario 1, the Faradaic reaction $\mathrm{Li}^+ + e^- \rightarrow \mathrm{Li}$ takes place at the the buffer/

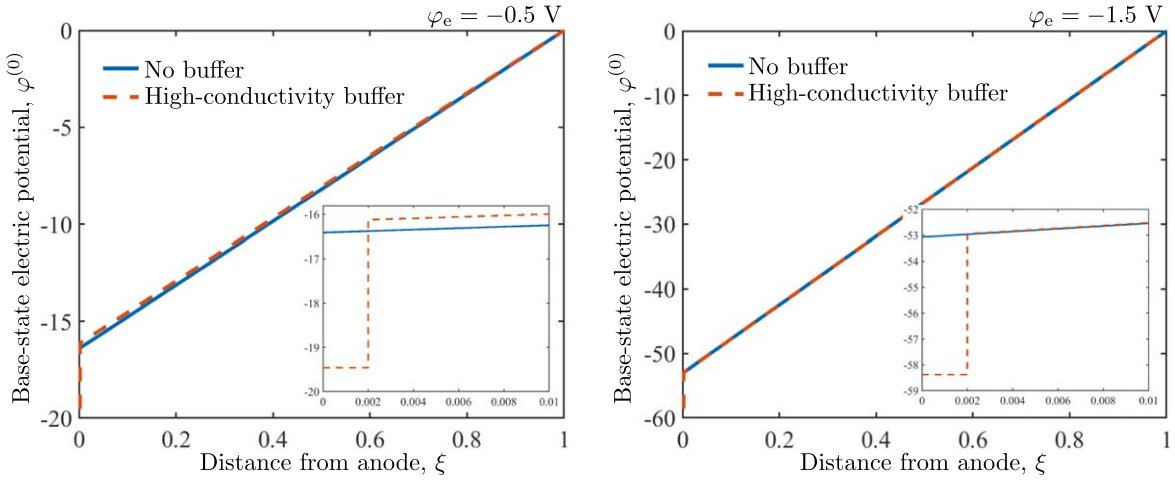

Figure A·1. Spatial profiles of the dimensionless base-state electric potential $\phi^{(0)}(\xi)$ in ASSBs without a buffer and with a high-conductivity buffer ($D_b = 1$ and $Ca_{Li}^{el} = Ca_{Li}^{b}$). These are plotted in the dimensionless moving coordinate system $\xi = x - Ut$, wherein ξ represents the distance from the growing electrode surface.

electrolyte interface and the electric potential in the buffer is constant.

The solutions for $\phi^{(0)}(\xi)$ and $c^{(0)}(\xi)$, and their first- and second-order derivatives, serve as coefficients in the perturbed-state BVPs, i.e., in Eqs. A·4–A·16 with $n = 1$. The latter are solved numerically[14] by employing a second-order finite-difference scheme and solving the resulting generalized eigenvalue problem with the Matlab function `eigs` to compute the dispersion relation $w = w(k)$. Alternatively, under certain assumptions, the perturbed-state BVPs for $\phi^{(1)}(\xi)$ and the dispersion relations from Eq. A·12 are solved analytically in Appendix B.

Appendix B. Analytical Dispersion Relations

B.1. Scenario 1: High-conductivity buffer.—Let us assume that $w \ll Dk^2$ in A·8 with $n = 1$, i.e., that the temporal fluctuations of the first-order perturbation $c^{(1)}(\xi)$ are negligible. This yields a PDE

$$\frac{d^2c^{(1)}}{d\xi^2} = k^2c^{(1)}, \qquad 0 < \xi < L_1, \tag{B·1}$$

whose solution is $c^{(1)}(\xi) = \beta_1 \exp(k\xi) + \beta_2 \exp(-k\xi)$. The constants of integration β_1 and β_2 are obtained from boundary conditions A·9,

$$D_b \frac{dc^{(1)}}{d\xi}(0) = R_\Gamma^{(1)}, \qquad D_b \frac{dc^{(1)}}{d\xi}(L_1) = R_{Li}^{(1)}. \tag{B·2}$$

Substituting this solution into Eq. A·12, and recalling that $zR_{Li}^{(0)} = I^{(0)}$, we obtain the dispersion relation

$$w = \frac{\omega c_0}{z} \frac{I^{(0)}/c^\Theta - D_b Ca_{Li}^b(\alpha_{cat} I^{(0)}/k_0 + z)k^2}{D_b/k_0 - B}, \tag{B·3a}$$

where

$$a = -\frac{k_0}{c^\Theta} e^{(1-\alpha_{cat})z\eta_\alpha^{(0)}}, \qquad A = \frac{a + D_b k}{a - D_b k} e^{2kL_1},$$
$$B = \frac{1}{c^\Theta k} \frac{1 - A}{1 + A}. \tag{B·3b}$$

The critical wavenumber, k_{cr}, is a wavenumber k for which $w = 0$. It follows from Eq. B·3a that

$$k_{cr} = \sqrt{\frac{I^{(0)}}{Ca_{Li}^b D_b c^\Theta(\alpha_{cat} I^{(0)}/k_0 + z)}}. \tag{B·4}$$

B.2. Scenario 2: Low-conductivity buffer.—The solution of BVPs A·4–A·7 and A·14–A·17 is

$$\varphi^{(1)} = A \begin{cases} \xi + (L_1 - 1)\frac{\sigma_b}{\sigma_{el}} - L_1 & 0 \leqslant \xi \leqslant L_1 \\ \frac{\sigma_b}{\sigma_{el}}(\xi - 1) & L_1 \leqslant \xi \leqslant 1, \end{cases} \tag{B·5a}$$

where

$$A = \frac{zh^{(1)}R_{Li}^{(0)} - k^2 h^{(1)} Ca_{Li}^b \sigma_b}{\sigma_b/K - z[(L_1 - 1)\sigma_b/\sigma_{el} - L_1]} \tag{B·5b}$$

and

$$K = k_0 e^{-\alpha_{cat} z\eta_\alpha^{(0)}}[(1 - \alpha_{cat})e^{z\eta_\alpha^{(0)}} + \alpha_{cat}]. \tag{B·5c}$$

Substituting Eq. B·5a into Eq. A·12, and recalling that $zR_{Li}^{(0)} = I^{(0)}$, yields the dispersion relation,

$$w = \omega c_0 \frac{I^{(0)} - k^2 Ca_{Li}^b \sigma_b}{\sigma_b/K - z[(L_1 - 1)\sigma_b/\sigma_{el} - L_1]}, \tag{B·6}$$

and the critical wavenumber,

$$k_{cr} = \sqrt{\frac{I^{(0)}}{Ca_{Li}^b \sigma_b}}. \tag{B·7}$$

In the absence of a buffer, $L_1 = 0$, $\sigma_b = \sigma_{el}$, and $\sigma_b = \sigma_{el}$. Hence, for ASSBs without a buffer, Eqs. B·6 and B·7 reduce to

$$w = \omega c_0 \frac{I^{(0)} - k^2 Ca_{Li}^{el} \sigma_{el}}{\sigma_{el}/K + z} \tag{B·8}$$

and the critical wavenumber k_{cr},

$$k_{cr} = \sqrt{\frac{I^{(0)}}{Ca_{Li}^{el} \sigma_{el}}}. \tag{B·9}$$

ORCID

Weiyu Li https://orcid.org/0000-0002-7857-8115
Daniel M. Tartakovsky https://orcid.org/0000-0001-9019-8935

References

1. R. Murugan, V. Thangadurai, and W. Weppner, "Fast lithium ion conduction in garnet-type $Li_7La_3Zr_2O_{12}$." *Angew. Chem. Int. Ed.*, **46**, 7778 (2007).

2. F. Shen, M. B. Dixit, X. Xiao, and K. B. Hatzell, "Effect of pore connectivity on Li dendrite propagation within LLZO electrolytes observed with synchrotron X-ray tomography." *ACS Energy Lett.*, **3**, 1056 (2018).
3. P. Barai, A. T. Ngo, B. Narayanan, K. Higa, L. A. Curtiss, and V. Srinivasan, "The role of local inhomogeneities on dendrite growth in LLZO-based solid electrolytes." *J. Electrochem. Soc.*, **167**, 100537 (2020).
4. D. Cao, X. Sun, Q. Li, A. Natan, P. Xiang, and H. Zhu, "Lithium dendrite in all-solid-state batteries: growth mechanisms, suppression strategies, and characterizations." *Matter*, **3**, 57 (2020).
5. S. Tang, G. Chen, F. Ren, H. Wang, W. Yang, C. Zheng, Z. Gong, and Y. Yang, "Modifying an ultrathin insulating layer to suppress lithium dendrite formation within garnet solid electrolytes." *J. Mater. Chem. A*, **9**, 3576 (2021).
6. Y. Luo, W. Feng, Z. Meng, Y. Wang, X. Jiang, and Z. Xue, "Interface modification in solid-state lithium batteries based on garnet-type electrolytes with high ionic conductivity." *Electrochimica Acta*, **397**, 139285 (2021).
7. Z. Zuo, L. Zhuang, J. Xu, Y. Shi, C. Su, P. Lian, and B. Tian, "Lithiophilic silver coating on lithium metal surface for inhibiting lithium dendrites." *Frontiers in Chemistry*, **8**, 109 (2020).
8. W. Li and D. M. Tartakovsky, "Effective representation of active material and carbon binder in porous electrodes." *J. Electrochem. Soc.*, **169**, 040556 (2022).
9. F. Boso, W. Li, K. Um, and D. M. Tartakovsky, "Impact of carbon binder domain on the performance of lithium-metal batteries." *J. Electrochem. Soc.*, **169**, 100550 (2022).
10. T. Nakamura, K. Amezawa, J. Kulisch, W. G. Zeier, and J. Janek, "Guidelines for all-solid-state battery design and electrode buffer layers based on chemical potential profile calculation." *ACS Appl. Mater. Interfaces*, **11**, 19968 (2019).
11. Z. Ahmad, T. Xie, C. Maheshwari, J. C. Grossman, and V. Viswanathan, "Machine learning enabled computational screening of inorganic solid electrolytes for suppression of dendrite formation in lithium metal anodes." *ACS Central Science*, **4**, 996 (2018).
12. M. H. Braga, N. S. Grundish, A. J. Murchison, and J. B. Goodenough, "Alternative strategy for a safe rechargeable battery." *Energy & Environmental Science*, **10**, 331 (2017).
13. H. Fang and P. Jena, "Li-rich antiperovskite superionic conductors based on cluster ions." *Proceedings of the National Academy of Sciences*, **114**, 11046 (2017).
14. W. Li, H. A. Tchelepi, Y. Ju, and D. M. Tartakovsky, "Stability-guided strategies to mitigate dendritic growth in lithium-metal batteries." *J. Electrochem. Soc.*, **169**, 060536 (2022).
15. M. C. Pang, Y. Hao, M. Marinescu, H. Wang, M. Chen, and G. J. Offer, "Experimental and numerical analysis to identify the performance limiting mechanisms in solid-state lithium cells under pulse operating conditions." *Phys. Chem. Chem. Phys.*, **21**, 22740 (2019).
16. F. Han, A. S. Westover, J. Yue, X. Fan, F. Wang, M. Chi, D. N. Leonard, N. J. Dudney, H. Wang, and C. Wang, "High electronic conductivity as the origin of lithium dendrite formation within solid electrolytes." *Nat. Energy*, **4**, 187 (2019).
17. S. D. Fabre, D. Guy-Bouyssou, P. Bouillon, F. Le Cras, and C. Delacourt, "Charge/discharge simulation of an all-solid-state thin-film battery using a one-dimensional model." *J. Electrochem. Soc.*, **159**, A104 (2011).
18. K. E. Thomas-Alyea, "Design of porous solid electrolytes for rechargeable metal batteries." *J. Electrochem. Soc.*, **165**, A1523 (2018).
19. F. Single, B. Horstmann, and A. Latz, "Theory of impedance spectroscopy for lithium batteries." *J. Phys. Chem. C*, **123**, 27327 (2019).
20. L. von Kolzenberg, A. Latz, and B. Horstmann, "Solid-electrolyte interphase during battery cycling: Theory of growth regimes." *ChemSusChem*, **13**, 3901 (2020).
21. L. G. Sundström and F. H. Bark, "On morphological instability during electrodeposition with a stagnant binary electrolyte." *Electrochimica Acta*, **40**, 599 (1995).
22. K. V. Kravchyk, F. Okur, and M. V. Kovalenko, "Break-even analysis of all-solid-state batteries with Li-garnet solid electrolytes." *ACS Energy Lett.*, **6**, 2202 (2021).
23. P. Gonzalez Puente, S. Song, S. Cao, L. Z. Rannalter, Z. Pan, X. Xiang, Q. Shen, and F. Chen, "Garnet-type solid electrolyte: Advances of ionic transport performance and its application in all-solid-state batteries." *Journal of Advanced Ceramics*, **10**, 933 (2021).
24. E. Rumble and R. John, *CRC Handbook of Chemistry and Physics* (CRC Press/Taylor & Francis, Boca Raton, FL) 102nd ed. (2021), (Internet Version 2021).
25. A. A. Talin, D. Ruzmetov, A. Kolmakov, K. McKelvey, N. Ware, F. El Gabaly, B. Dunn, and H. S. White, "Fabrication, testing, and simulation of all-solid-state three-dimensional Li-ion batteries." *ACS Appl. Mater. Interfaces*, **8**, 32385 (2016).
26. H.-K. Tian, Z. Liu, Y. Ji, L.-Q. Chen, and Y. Qi, "Interfacial electronic properties dictate Li dendrite growth in solid electrolytes." *Chemistry of Materials*, **31**, 7351 (2019).
27. M. Morey, J. Loftus, A. Cannon, and E. Ryan, "Interfacial studies on the effects of patterned anodes for guided lithium deposition in lithium metal batteries." *J. Chem. Phys.*, **156**, 014703 (2022).
28. J. Suzuki, K. Sekine, and T. Takamura, "Evaluation of the diffusion coefficient of Li in Ag using a Li+ sensor electrode mounted in a bipolar cell." *Electrochemistry*, **74**, 303 (2006).
29. J. Willhite, N. Karnezos, P. Cristea, and J. Brittain, "Li7 self diffusion in LiAl—an NMR study." *J. Phys. Chem. Solids*, **37**, 1073 (1976).
30. T. Zhang, L. Fu, J. Gao, Y. Wu, R. Holze, and H. Wu, "Nanosized tin anode prepared by laser-induced vapor deposition for lithium ion battery." *Journal of Power Sources*, **174**, 770 (2007).
31. W. Tyson and W. Miller, "Surface free energies of solid metals: estimation from liquid surface tension measurements." *Surf. Sci.*, **62**, 267 (1977).
32. F. C. Walsh, "Electrode reactions in metal finishing." *Transactions of the IMF*, **69**, 107 (1991).
33. G. Kaptay, "Method for estimating solid-solid interface energies in metal-ceramic systems: the aluminium-silicon carbide system." *Materials Science Forum*, **215-216**, 475 (1996).
34. K. Shen, Y. Wang, J. Zhang, Y. Zong, G. Li, C. Zhao, and H. Chen, "Revealing the effect of grain boundary segregation on Li ion transport in polycrystalline antiperovskite Li_3ClO: a phase field study." *Phys. Chem. Chem. Phys.*, **22**, 3030 (2020).
35. K. Fu et al., "Toward garnet electrolyte-based Li metal batteries: an ultrathin, highly effective, artificial solid-state electrolyte/metallic Li interface." *Sci. Adv.*, **3**, e1601659 (2017).
36. M. He, Z. Cui, C. Chen, Y. Li, and X. Guo, "Formation of self-limited, stable and conductive interfaces between garnet electrolytes and lithium anodes for reversible lithium cycling in solid-state batteries." *J. Mater. Chem.*, A**6**, 11463 (2018).
37. K. Fu, Y. Gong, Z. Fu, H. Xie, Y. Yao, B. Liu, M. Carter, E. Wachsman, and L. Hu, "Transient behavior of the metal interface in lithium metal-garnet batteries." *Angew. Chem. Int. Ed.*, **56**, 14942 (2017).
38. X. Han, Y. Gong, K. K. Fu, X. He, G. T. Hitz, J. Dai, A. Pearse, B. Liu, H. Wang, and G. Rubloff, "Negating interfacial impedance in garnet-based solid-state Li metal batteries." *Nat. Mater.*, **16**, 572 (2017).
39. H. Xu, Y. Li, A. Zhou, N. Wu, S. Xin, Z. Li, and J. B. Goodenough, "Li3N-modified garnet electrolyte for all-solid-state lithium metal batteries operated at 40 ° C." *Nano Lett.*, **18**, 7414 (2018).
40. X. Fan, X. Ji, F. Han, J. Yue, J. Chen, L. Chen, T. Deng, J. Jiang, and C. Wang, "Fluorinated solid electrolyte interphase enables highly reversible solid-state Li metal battery." *Sci. Adv.*, **4**, 9245 (2018).
41. C. Kwon and D. M. Tartakovsky, "Modified immersed boundary method for flows over randomly rough surfaces." *J. Comput. Phys.*, **406**, 109195 (2020).
42. D. Xiu and D. M. Tartakovsky, "Numerical methods for differential equations in random domains." *SIAM Journal on Scientific Computing*, **28**, 1167 (2006).
43. D. M. Tartakovsky and D. Xiu, "Stochastic analysis of transport in tubes with rough walls." *J. Comput. Phys.*, **217**, 248 (2006).